Induction of planar Li growth with designed interphases for dendrite-free Li metal anodes

Xiang Han [a], Jizhang Chen [a,*], Minfeng Chen [a], Weijun Zhou [a], Xiaoyan Zhou [a], Guanwen Wang [a], Ching-Ping Wong [b,*], Bo Liu [c,*], Linshan Luo [d], Songyan Chen [d], Siqi Shi [e]

[a] College of Materials Science and Engineering, Co-Innovation Center of Efficient Processing and Utilization of Forestry Resources, Nanjing Forestry University, Nanjing 210037, China
[b] School of Materials Science and Engineering, Georgia Institute of Technology, Atlanta, United States
[c] College of Mathematics and Physics, Jinggangshan University, Ji'an 343009, China
[d] Department of Physics, Xiamen University, Xiamen 361005, China
[e] School of Materials Science and Engineering, Shanghai University, Shanghai 200444, China

ARTICLE INFO

ABSTRACT

Lithium metal is the ultimate anode candidate for high-energy-density lithium batteries because of its high specific capacity (3860 mAh g^{-1}) and low redox potential (-3.05 V vs. SHE). The nonuniform lithium ions flux and the highly reactive nature of Li metal, however, lead to continuous Li dendrite formation and dead Li growth. In this work, a separator modified by two-dimensional layered MXene (Ti_3C_2-T, T=-O and -F) and the solid-state electrolyte $Li_{1.3}Al_{0.3}Ge_{1.7}(PO_4)_3$ (LAGP) is designed to induce planar Li plating with engineered interphases. The highly mixed conductive nature of LAGP/MXene facilitates the uniform transfer of the lithium ions/electrons. In addition, the -O and -F groups provide more plating sites and lower the Li's initial nucleation energy, which laterally induce planar deposition. The rearrangement of Li atoms inherits the atomic structure of MXene and significantly suppresses the formation of dendritic Li. Furthermore, the in situ formed Ge, Li_3PO_4 and LiF interphases, originating from the reduction of LAGP, help to stabilize the solid electrolyte interphase (SEI). The LAGP/MXene-modified separator reduces the voltage hypothesis and enables stable Li metal plating and stripping. In a full cell with a high loading of $LiCoO_2$ (20 mg cm^{-2}), the engineered separator exhibits stable cycling performance after 200 cycles. The novel strategy of regulating Li deposition and engineering SEIs is facile and efficient and can be applied to other alkali metal anodes.

1. Introduction

Lithium metal is the ultimate anode candidate for high-energy-density lithium batteries because of its high specific capacity (3860 mAh g^{-1}) and low redox potential (-3.05 V vs. SHE) [1-4]. Li dendrite growth induced by inhomogeneous Li plating/stripping, however, causes serious safety concerns and prohibits its practical applications [5-7]. Moreover, the low coulombic efficiency, originating from a severe Li/electrolyte reaction and an infinite volume change, results in rapid capacity degradation [8-10]. Normally, the separator skeleton is electron insulating but can transport lithium ions through its pores between the cathode and anode. The anisotropic distribution of Li ions on the anode surface results in the inhomogeneous nucleation and deposition of Li ions and dendritic Li growth. Non-reactive solid electrolyte coatings that can uniformly coat the lithium ions on anode surfaces, such as lithium lanthanum zirconium tantalum oxide (LLZTO) and lithium

lanthanum zirconium oxide (LLZO), were evaluated [11-13]. However, the poor wettability of this kind of solid electrolyte retards the rapid transfer of lithium ions and leads to a high interfacial impedance. In addition, the solid electrolyte interphase (SEI) formed in carbonate electrolytes still suffers from nonuniform lithium-ion flux and poor mechanical stability [1,14]. Electrolyte engineering, including using fluorinated solvents, high-concentration electrolytes, $AlCl_3$, $LiNO_3$, lithium bis(trifluoromethanesulfonyl)imide (LiTFSI) additives and so on, is an effective route to improve the mechanical strength of SEIs on Li metal [15-17]. Building an artificial protective layer is another way to improve the distribution of composites in the SEI, providing fast Li-ion diffusion and increasing the mechanical strength [18–21].

More recently, researchers have paid more attention to structured and functionalized conductive Li hosts to induce planar Li deposition. For example, graphene, nitrogen-doped graphene [22], three-dimensional (3D) porous copper [23], metal-organic frameworks
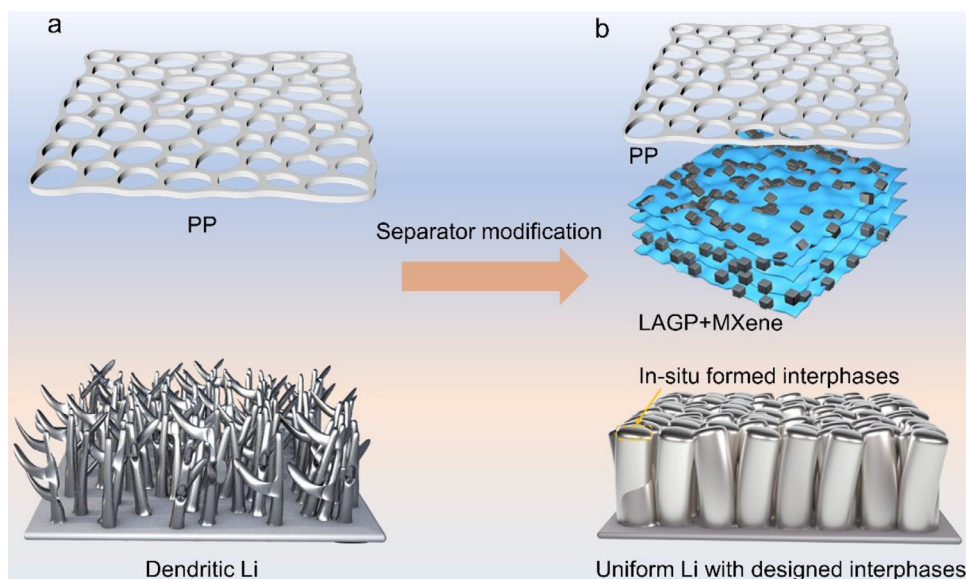

Fig. 1. Schematic of the LAGP/MXene-modified separator. (a) Dendritic Li deposition using a traditional porous PP separator. (b) Uniform planar-like Li deposition with designed stable interphases using the modified separator.

(MOFs) [24], vertically aligned nanoscale channels [25], and 3D structures containing nanopores [26] have been designed to regulate the deposition of Li ions. The large specific surface area of these conductive frameworks lowers the local current density. In addition, a functionalized two-dimensional (2D) material that can effectively reduce the nucleation energy barrier and induce even deposition should be designed. MXene (Ti_3C_2-*T*, *T* represents functional groups), as a new 2D layered material, has abundant surface functional groups, a high electronic conductivity, and a high mechanical strength [27,28]. MXenes applied in composite Li metal anodes, such as structured MXene-Li films, MXene aerogels, and pillared Sn@MXene, show better cycling stability due to suppressed dendritic Li/Na growth and a good affinity between the surface functional groups and Li/Na metals [29-31]. However, the induction mechanism of Li metal growth on MXenes is still unclear.

In this work, regarding the demands of uniform Li deposition and robust mechanical strength of the SEI layer, we propose a separator modified by a $Li_{1.3}Al_{0.3}Ge_{1.7}(PO_4)_3$ (LAGP) and Ti_3C_2-*T* (*T*=-O and -F) composite (Fig. 1). In the composite, MXene and LAGP supply fast electron and lithium-ion channels, respectively. In addition, the O and F groups on MXene promote Li nucleation and laterally induce oriented deposition, which is demonstrated by density functional theory (DFT) calculations and experimental results. As a result, Li atoms are directly deposited from the MXene side to the Li metal substrate side with a "sheet-like" structure. Furthermore, LAGP can react with Li metal to form stable interphases comprising Li_3PO_4, LiF, and Ge. Taking advantage of the designed SEI and uniform Li deposition, a high-rate and long-durable cycling performance are achieved. For example, Li/Li cells show superior performance with an accumulated capacity of 1000 mAh cm^{-2}. In a full cell with the engineered separator, even at a high cathode loading of 20 mg cm^{-2} $LiCoO_2$ (LCO), the cell shows a high capacity retention after 200 cycles. In our work, a new principle for designing stable alkali metal anodes is developed.

2. Results and discussion

Scanning electron microscopy and transmission electron microscopy (SEM and TEM, respectively) were used to characterize the morphology of LAGP and MXene. Ti_3C_2-*T* nanosheets were synthesized by etching MAX-Ti_3AlC_2 and were confirmed by X-ray diffraction patterns with the observation of a (002) peak (Figure S1). After a two-step centrifugal separation process, few-layer Ti_3C_2-*T* was obtained (Figure S2). Fig. 2(a) shows the surface SEM image of the LAGP/MXene-coated polypropylene (PP) separator. Nanosized LAGP powders are well dispersed on the

MXene sheets, which fully cover the porous PP separator. The interconnected 2D MXene exhibits a uniform surface electrical field distribution and laterally induces uniform Li metal deposition. Note that lithium ions are transported slowly across different MXene sheets. Thus, lithium-ion conductor LAGP nanoparticles, the X-ray diffraction (XRD) patterns of which are shown in Figure S3, are incorporated into the space between the different layers of MXene and the pores. LAGP shows a high ionic conductivity of ~ 5×10^{-4} S cm^{-2} at room temperature (Figure S4). As a result, the LAGP/MXene provides a fast electron and lithium-ion transport pathway across the separator surface. The thickness of the LAGP/MXene composite coating layer is approximately 7 μm (Figure S5). Fig. 2(b) shows the TEM image of the LAGP/MXene composite. Nanosized LAGP particles are embedded on the flexible MXene sheet with shrinkage, while some crimping parts are observed on the edge. The crystalline structure of MXene was examined by high-resolution TEM (HRTEM, Fig. 2c), and the number of MXene layers was 4 with a plane spacing of 0.99 nm, corresponding to the (002) planes of Ti_3C_2-*T* [32]. In the inner parts of the MXene pieces, a hexagonal crystalline structure is observed, and the interplanar space is 0.21 nm. The HRTEM of LAGP shows that the interplanar spacing is 0.36 nm (Fig. 2d), corresponding to its (113) planes [33].

A dark-field TEM image of LAGP/MXene is shown in Fig. 2(e), and the LAGP nanoparticles are enrolled in the flexible MXene framework. The elemental energy dispersive spectroscopy (EDS) mapping, shown in Fig. 2(f), further confirms that the LAGP particles are embedded in the flexible MXene nanosheets. Notably, O and F signals are also detected at the surface of MXene (see detailed EDS mapping information in Figure S6), indicating the terminal functional groups of -F and -O.

To reveal the lithium transportation mechanism and to test the ionic conductivity, lithium-ions-blocking stainless steel (SS) was used as current collector and SS/Separator/SS cells were fabricated. As shown in Figures S7a and b, the resistance of PP and PP/MXene are the same and smallest (1.4 Ω), implying the lithium ions transportation in the coating layer is short by high electronically conductive MXene. In this case, Li metal could deposit on the top side of MXene coating layer. However, the resistance of PP/LAGP+MXene is 2.7 Ω, revealing that the lithium ions can transport at the top side of the composite coating layer and is not short by electrons; and partially lithium ions transportation (at the bottom side) is short by MXene. This is because the resistance of PP/LAGP is 4.3 Ω, which is higher than that of PP/LAGP+MXene. However, the lithium ions at the top side mainly transport through the bulk phase of LAGP and the interface of liquid electrolyte and LAGP [34] between the adjacent two layers of MXene; and through the defects of
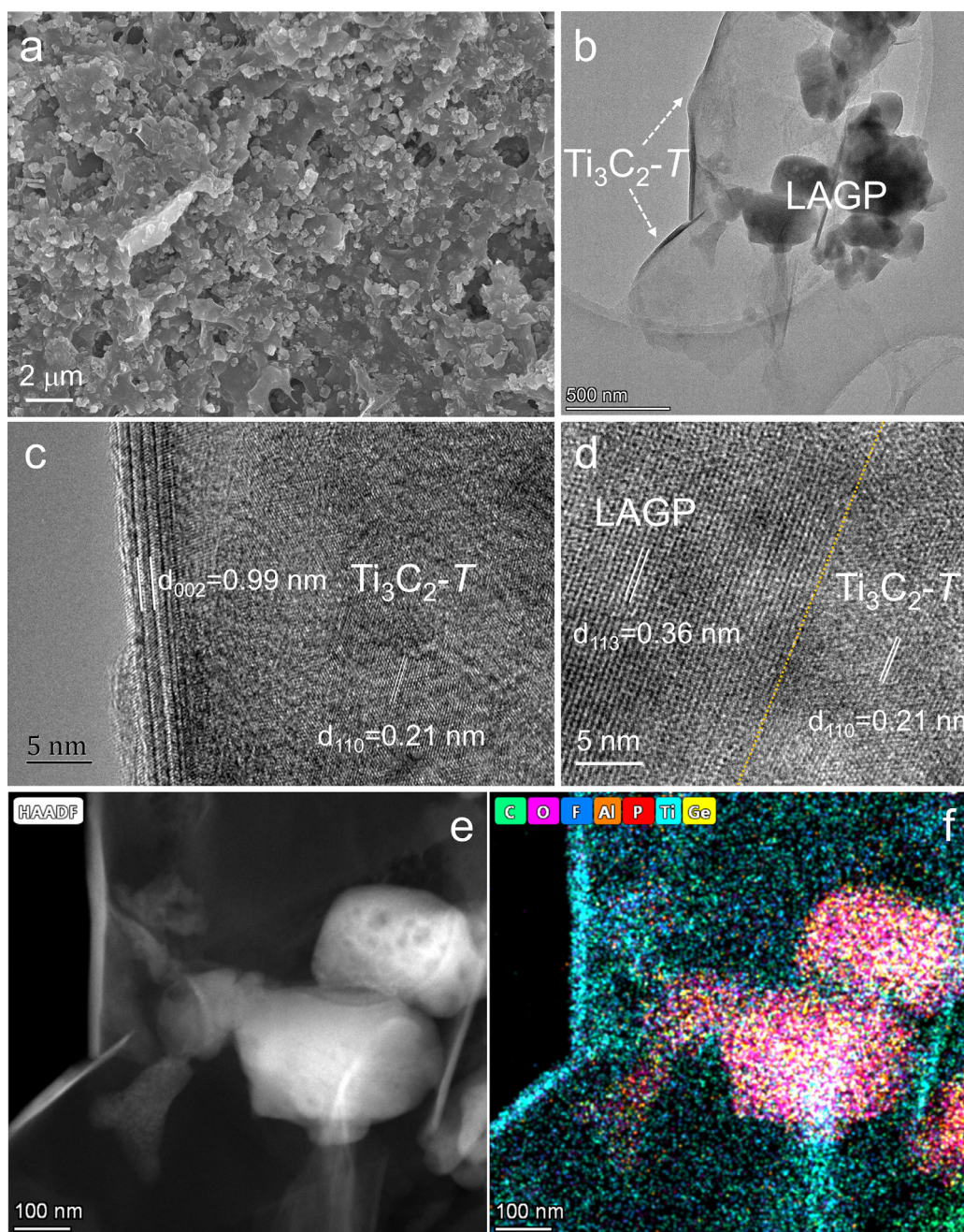
Fig. 2. Synthesis and characterization of the LAGP/MXene composite coating layer. (a) Surface SEM image of the LAGP/MXene coating layer. (b) TEM image of the LAGP/MXene composite. (c) High-resolution TEM image of MXene. (d) High-resolution TEM image of LAGP/MXene. (e) Dark-field TEM image of LAGP/MXene. (f) EDS mapping of LAGP/MXene in (e).

MXene between different layers. With an optimized ratio, the electronical conductivity from the bottom side to the top side is gradually decreased, which induces planar lithium metal deposition from the bottom side of the composite coating layer to the lithium metal substrate. The design principles here is different from Li metal coating, for which normally highly conductive host structures were used, such as pure MXene, Graphene, and RGO [31,35,36]. More importantly, separator coating is facile and compatible with traditional slurry cast method.

To estimate the electrochemical stability of the LAGP/MXene-modified PP separator against lithium metal, the mass ratio of LAGP to MXene is 8:1 if not mentioned. Symmetric Li/Li metal electrodes were assembled into a coin-type cell with carbonate liquid electrolyte. Under an area capacity of 1 mAh cm^{-2}, the symmetric cells with PP/LAGP+MXene separators demonstrate a stable Li plating/stripping voltage until 700 h under a current density of 1 mA cm^{-2} (Fig. 3a). By contrast, the cell with the pristine PP separator shows an obvious voltage increase after 200 h, as shown in Figs. 3(a) and (b). The voltage hysteresis of the cells with PP and PP/LAGP+MXene are 0.43 and 0.023 V, respectively. This result is because of the large interfacial resistance caused by dead lithium and mossy Li with poor interconnections. At a higher area capacity of 2 mAh cm^{-2} per cycle, the same trend is also observed (Figs. 3c and d). The cell with PP/LAGP+MXene shows stable cycling after 1000 h, while the cell with the PP separator shows an obvious voltage hysteresis increase after 250 h. The voltage peaks of cells used PP separator in Figs. 3b and d is because a thick film of dendrites formed after repeated deposition and stripping processes, during which the lithium metal transformed to mossy structure with tiny dendrites. At the same time, the highly reactive lithium dendrites
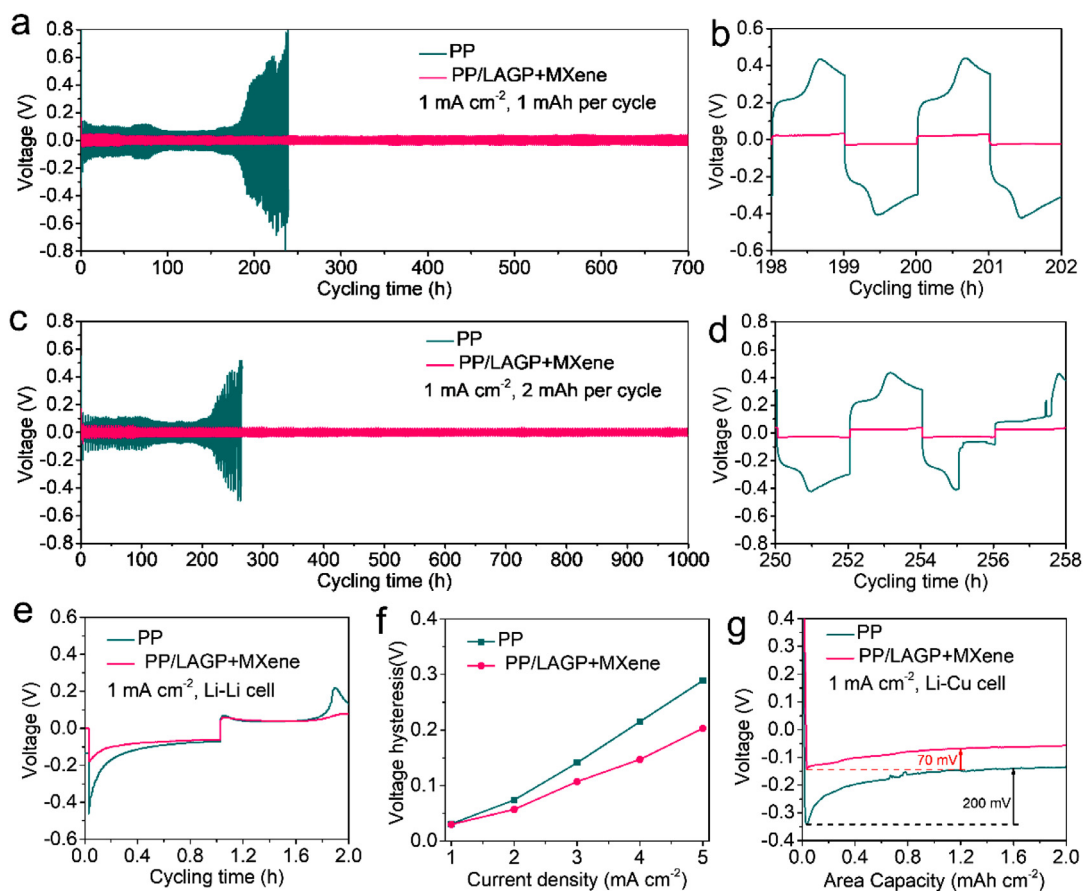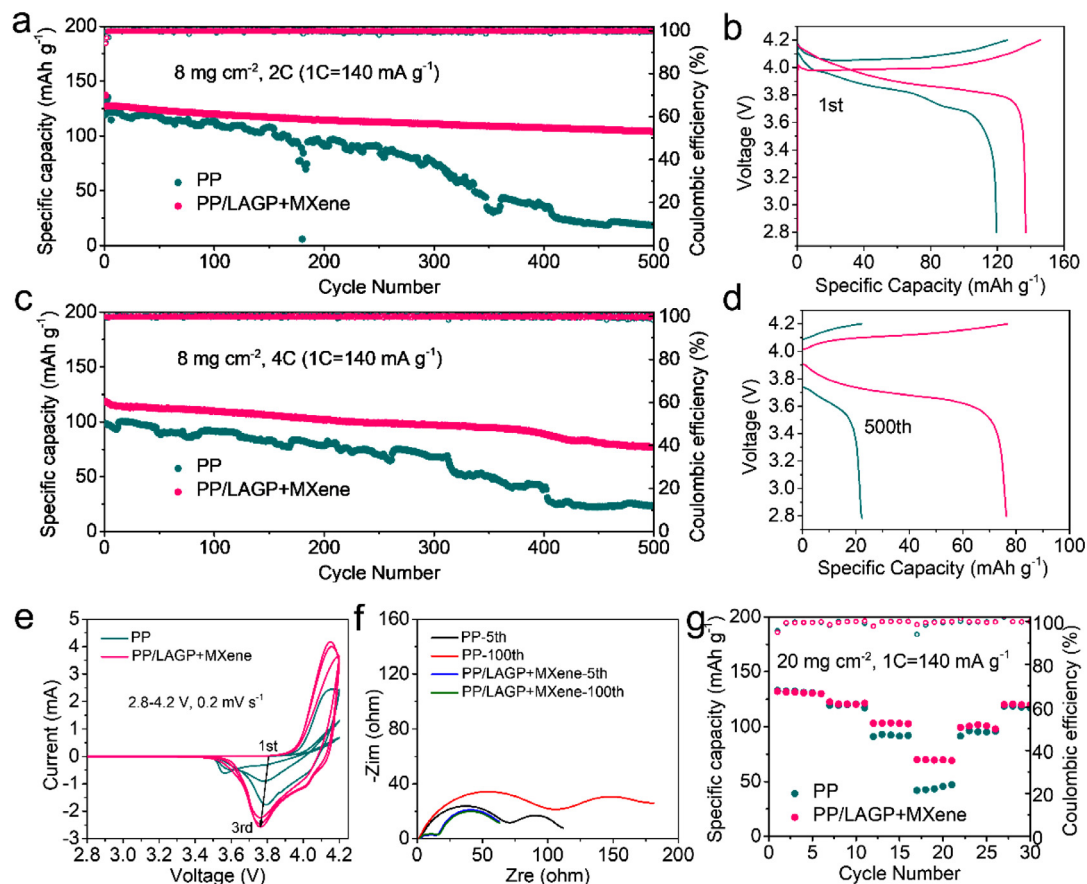
Fig. 3. Electrochemical performance of Li/Li symmetric cells with PP and PP/LAGP+MXene separators. (a) Voltage-time profiles of Li plating/stripping with an area capacity of 1 mAh cm^{-2} at 1 mA cm^{-2}. (b) The amplified profiles in (a). (c) Voltage-duration time profiles of Li plating/stripping with an area capacity of 2 mAh cm^{-2} at 1 mA cm^{-2}. (d) The amplified profiles in (c). (e) The initial voltage-time profiles of Li plating/stripping with an area capacity of 1 mAh cm^{-2} at 1 mA cm^{-2}. (f) Voltage hysteresis of Li/Li symmetric cells at 1, 2, 3, 4, and 5 mA cm^{-2} with a single side-coated separator. (g) Voltage-capacity profile of the Li-Cu cell at 1 mA cm^{-2}.

react with liquid electrolyte and formed SEI layer, which is insulated and irreversible (also called 'dead lithium'). Due to the poor mechanical property of lithium dendrites, the dendrites coated with insulated layer may peel off the lithium metal substrate, and the polarization voltage increased. After that, newly dendrites formed and the effective electrochemical reactive area increased and the polarization voltage decreased. The initial voltage-time profiles of Li plating/stripping show that the cell with the LAGP/MXene-modified separator has a smaller nucleation overpotential (Fig. 3e). Derived from the voltage-time profiles in Figure S8, the voltage hysteresis of Li-Li symmetric cells with the PP separator are 0.03, 0.074, 0.141, 0.215, and 0.289 V at 1, 2, 3, 4, and 5 mA cm^{-2} (Fig. 3f), respectively. The Li-Li cells with the PP/LAGP+MXene separator show smaller overpotentials of 0.03, 0.057, 0.107, 0.147, and 0.203 V at 1, 2, 3, 4, and 5 mA cm^{-2} (Fig. 3f), respectively. This finding indicates that LAGP/MXene benefits the kinetics of Li deposition and stripping due to fast lithium-ion and electron transportation at the interface between LAGP/MXene and the Li metal. In addition, good wettability between the liquid electrolyte and separator may help to enhance the rate performance. As shown in Supplementary Video 1, the carbonate liquid electrolyte can easily permeate the PP/LAGP+MXene separator within one second, confirming the good affinity of the modified separator with the liquid electrolyte. In contrast, the contact angle between PP and the same liquid electrolyte is approximately 43.3° (Figure S9). Furthermore, the large number of terminal -O and -F groups can reduce the energy barrier of Li nucleation and induce Li metal deposition. The fast kinetics enabled by the LAGP/MXene coating is further demonstrated by Li-Cu cells; for example, the over-

potentials of cells with PP and PP/LAGP+MXene are 200 and 70 mV (Fig. 3g), respectively. We also tested the electrochemical performance of the Li/Li cell with a PP/LAGP separator (Figure S10) as a comparison. The LAGP coating enabled stable cycling performance for 300 h, further demonstrating the synergetic effects of the LAGP/MXene composite coating for improving the stability and fast kinetics against the Li metal.

To explore the application of LAGP/MXene-modified separators in full lithium metal batteries, LCO/Li practical cells were assembled. At a loading of 8 mg cm^{-2}, the initial capacities of the cells with PP and PP/LAGP+MXene tested at 0.5C (1C=140 mA g^{-1}) are 119.5 and 137 mAh g^{-1} (Figs. 4a and b), respectively. The cell with PP shows a lower capacity because of its slow Li plating/stripping kinetics; for example, the overpotentials for PP and PP/LAGP+MXene are 0.24 and 0.11 V (Fig. 4b), respectively. Nonetheless, during the initial stage of the first charge process, the starting voltages are 4.16 and 4.0 V (Fig. 4b), further demonstrating the smaller energy barrier for Li plating after coating with LAGP/MXene. After 2 cycles activated at 0.5C, the cell was then subjected to a long-life test at 2C. The cell with the PP separator starts to degrade after 200 cycles, and the capacity retention is only 18.2 mAh g^{-1} after 500 cycles. In sharp contrast, the cell with the LAGP/MXene-modified separator exhibits stable cycling performance for 500 cycles with a capacity of 100 mAh g^{-1}. Even at a high rate of 4C, the cell with the LAGP/MXene separator still shows stable cycling performance (Fig. 4c). The specific capacities of the cells with PP and PP/LAGP+MXene separators after 500 cycles are 23.2 and 76.7 mAh g^{-1} (Fig. 4c and d), respectively. The LAGP/MXene coating layer fa-

Fig. 4. Electrochemical performance of LCO/Li cells with PP and PP/LAGP+MXene separators. (a) The cycling performance of LCO/Li cells with different separators. The loading is 8 mg cm^{-2}, and the rate is 2C (1C=140 mA g^{-1}). (b) The initial charge-discharge profiles in (a). (c) The cycling performance of LCO/Li cells with different separators. The loading is 8 mg cm^{-2}, and the rate is 4C (1C=140 mA g^{-1}). (d) The initial charge-discharge profiles in (c). (e) The CV curves of LCO/Li cells at 0.2 mV s^{-1} between 2.8–4.2 V. (f) EIS plots of LCO/Li cells with different separators after 5 and 100 cycles. (g) The rate performance of LCO/Li cells with different separators.

cilitates fast lithium-ion transportation and may help to form a stable protecting layer on the Li metal surface.

To better prove the effect of LAGP nanoparticles, the electrochemical performance of a full cell used LAGP/MXene (1:1) coating layer modified PP separator was tested (Figure S11). After the initial two cycles tested at 0.5C, the cell was undergoing long-life test at 2C (Figure S11a). The initial discharge capacity is 136.4 mAh g^{-1} (Figure S11b), the overpotential is smaller compared to LAGP/MXene (8:1, Fig. 4b) due to more Li nucleation sites provided by lots of MXene. Before 300 cycles, the cell shows relative stable cycling performance and the specific capacity at 300th cycle is 102.2 mAh g^{-1}. After that, the capacity starts to fade quickly, and the capacity retention is only 70.8 mAh g^{-1} at 500th cycle. The cycling stability here is worse compared to LAGP/MXene (8:1) shown in Fig. 4a. With more MXene, the conductivity of the whole coating layer including the top surface significantly improved, the Li ions on the top side could easily be reduced and Li metal directly deposit on the top surface. By contrast, with only 10 wt.% MXene, the electronic conductivity of the composite coating layer should be gradient decreased from the bottom to the top side because of the insulated LAGP particles embedded between different MXene layers. With an optimized ratio, the lithium ions preferably to deposit on the bottom side of the composite coating layer, which could substantially improve the cycling stability.

Cyclic voltammetry (CV) at a scan rate of 0.2 mV s^{-1} was also carried out, as shown in Fig. 4e, to record the redox potential of the LCO/Li metal battery. For the cell with the PP separator, the redox currents increase with the cycle number, implying the activation process of Li metal. By contrast, the redox peaks almost overlap for the

first three cycles, indicating fast Li-ion transportation at the interface between LAGP/MXene and Li metal. Electrochemical impedance spectroscopy (EIS) was used to analyze the impedance evolution after different cycles, as shown in Fig. 4f. All Nyquist plots comprised two semicircles: the interfacial resistance at high frequency and the charge transfer resistance at low frequency. Obviously, the impedance of the cell with the PP separator is larger than that with the PP/LAGP+MXene separator after 5 cycles. In addition, the impedance is almost the same after 100 cycles for PP/LAGP+MXene, while it increases quickly for PP during the 100 cycles. The fast kinetics should enable the high-rate performance of the LCO/Li battery even at a high active mass loading of 20 mg cm^{-2}. The rate performance was tested between 0.5 and 4C (Fig. 4g). The specific capacities for the cell with the PP separator at 0.5, 1, 2, and 4 C were 130.9, 120.6, 91.5, and 45.5 mAh g^{-1}, respectively. The capacity at high rates significantly improved with LAGP/MXene modification; for example, the specific capacities were 130.9, 120.6, 91.5, and 45.5 mAh g^{-1} at 0.5, 1, 2, and 4 C, respectively. Our full cells with PP/LAGP+MXene separators further confirm the stable interphase layer and fast kinetics enabled by the LAGP/MXene coating.

To meet a high energy density, such as 300–500 Wh kg^{-1}, a high loading area capacity of 3–5 mAh cm^{-2} is required [37]. In our cases, LCO cathodes with a high loading of 20 mg cm^{-2} were fabricated and tested between 2.8–4.2 V. At a low rate of 0.1C (1C=140 mA g^{-1}), the initial capacities of cells with PP and PP/LAGP+MXene separators were 140.3 and 145 mAh g^{-1} (Figs. 5a and b), respectively. At 0.5C, both cells show relatively stable cycling during the first 100 cycles after the initial two cycles were activated at 0.1C (Fig. 5a). For the cell with the
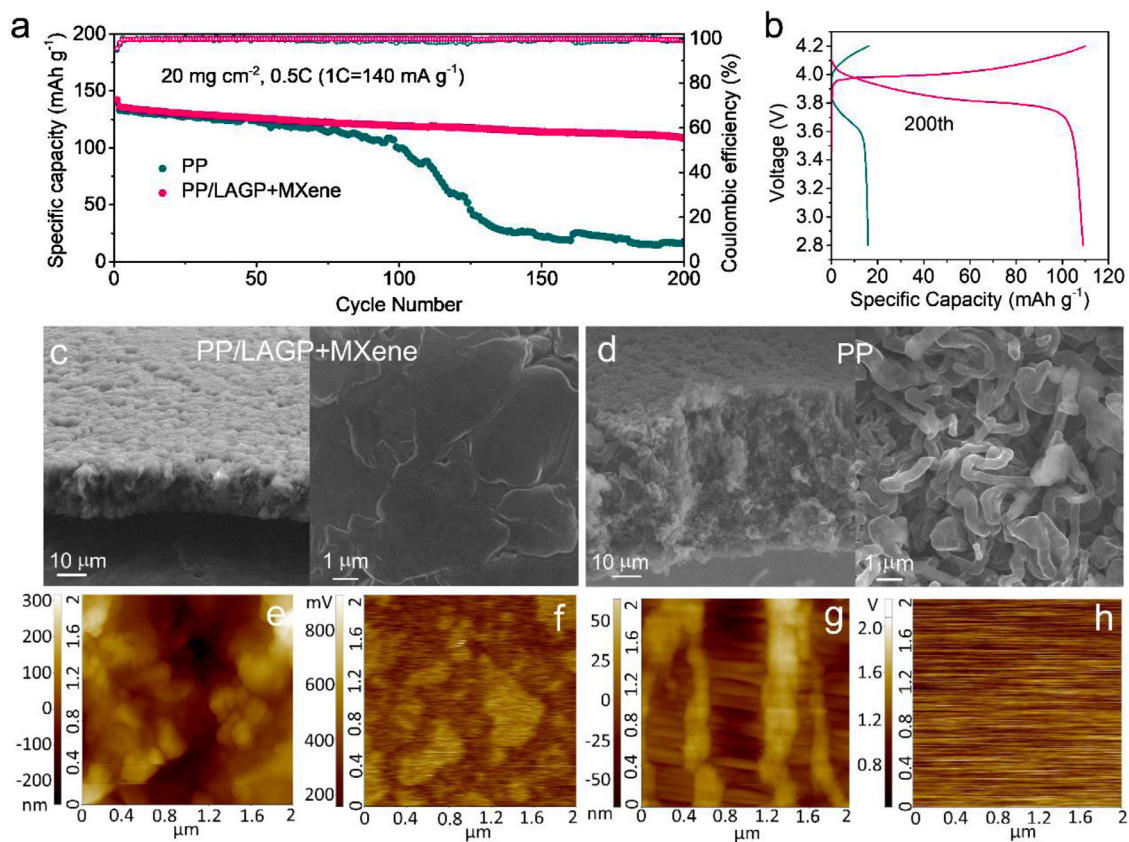
Fig. 5. Cycling performance and Li deposition with high loading LCO. (a) The cycling performance of LCO/Li cells with a high loading of 20 mg cm^{-2} at 0.5C and 1C=140 mA g^{-1}. (b) Voltage-capacity profiles of LCO/Li cells at the 200th cycle. (c) Cross-sectional and surface SEM images of the deposited Li metal in (a) with the PP/LAGP+MXene separator. (d) Cross-sectional and surface SEM images of the deposited Li in (a) with the PP separator. (e) AFM image of the PP/LAGP+MXene separator. (f) EFM image shows the surface electric field distribution of PP/LAGP+MXene. (g) AFM image of the PP separator. (h) EFM image shows the surface electric field distribution of PP separator.

PP separator, serious capacity degradation is observed after 100 cycles, and the capacity retention is only 15.9 mAh g^{-1} after 200 cycles (11.3% of the first cycle). Remarkably, the full cell with the LAGP/MXene-modified separator exhibits enhanced cycling stability. Even after 200 cycles, the specific capacity still retains 99 mAh g^{-1}, which is 68.3% of the first cycle. The LAGP/MXene-coated separator shows great potential in the practical application of high-area-capacity Li metal batteries.

The characterization of the Li metal morphology evolution in full cells is important to clarify the effect of the LAGP/MXene coating layer on the Li metal. From the cross-sectional SEM image (Fig. 5c), a dense structure is observed with a thickness of 18 μm. From the surface SEM image, densely stacked Li metal is observed, which further demonstrates that large Li sheets are formed. In contrast, the full cell with the PP separator shows a mossy and porous structure of the Li metal anode with a thickness of 50 μm (Fig. 5d). Many Li dendrites are formed on the surface of Li metal. Notably, the thickness of the pure Li film is 14 μm for 2.8 mAh cm^{-2}, so the volume expansion of the Li metal anodes with PP and PP/LAGP+MXene separators are 257% and 28%, respectively. The uniform and dense Li plating and stripping was attributed to the uniform Li-ion and electron transport enabled by LAGP/MXene. The large surface area of mossy Li leads to serious side reactions with the carbonate electrolyte and thick SEI coated on the Li dendrites during repeated cycles. As a result, the resistance continuously increases and loses the electrochemical activity of the Li metal, which causes fast capacity fading. Atomic force microscopy (AFM) was used to record the morphology and electrical field change after coating with LAGP/MXene. The nanosized LATP/MXene powders uniformly cover the PP surface, and no pores exist (Fig. 5e). From the electrostatic force microscopy (EFM) image, the voltage distribution is almost the same as the MXene morphology, and the electrical field does not change very much between different MXene sheets (Fig. 5f). However, large pores are observed in the skeleton of the PP separator (Fig. 5g). No voltage signal is detected on the PP separator (Fig. 5h), implying its insulating nature.

To better understand the guided deposition effects of Ti$_3$C$_2$-T ($T = -O$ and $-F$), first-principles calculations were employed to analyze the effective sections of Ti$_3$C$_2$-T. Ti$_3$C$_2$-T exhibited low adsorption energies for the first layer of Li (Ti$_3$C$_2$−O at −1.52 eV and Ti$_3$C$_2$−F at −0.58 eV), indicating a good affinity between Ti$_3$C$_2$-T and Li and confirming the low nucleation overpotential (Figs. 6a and c). When the number of Li layers reached 6 (Ti$_3$C$_2$−O) and 2 (Ti$_3$C$_2$-F), the adsorption energies gradually stabilize as the number of Li layers increase, and the corresponding adsorption energies are −0.35 eV and −0.13 eV, respectively. This result suggests that Ti$_3$C$_2$−O plays a more important role in inducing deposition than Ti$_3$C$_2$-F. In addition, the charge density difference plots of Li atom layer deposition on Ti$_3$C$_2$-T are shown in Figs. 6b and d, with yellow and blue areas representing electron gain and loss. An obvious blue area emerging above the first layer of Li atoms indicates a significant charge transfer from Li to the Ti$_3$C$_2$-T substrate. The large portion of yellow areas located on the O atoms illustrates that O atoms are the main electron acceptors. The above results reveal the fundamental protection mechanism by which Ti$_3$C$_2$-T could efficiently induce Li atom stable deposition and the formation of a homogeneous electrode surface.

The thermodynamic phase stability of LAGP/Li was evaluated by DFT calculations. The reaction energy between LAGP and Li is shown in Fig. 7(a), and the large negative Gibbs free energy value implies that
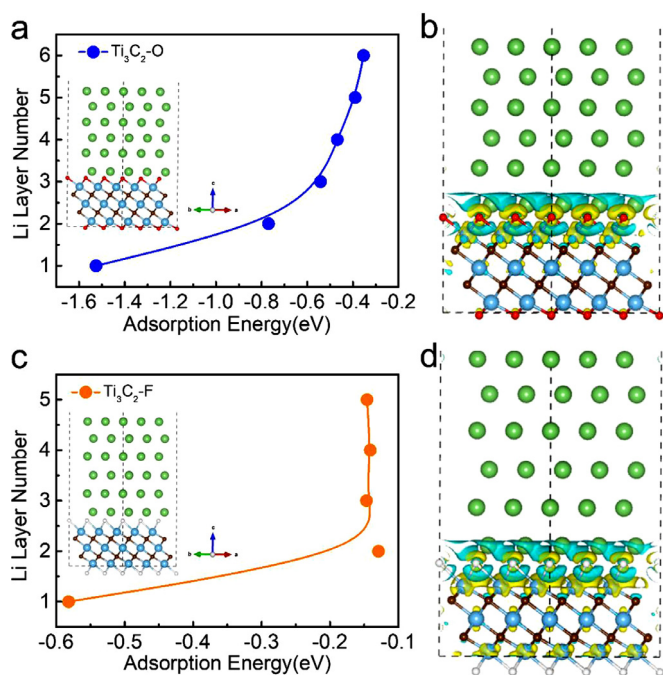
Fig. 6. The mechanism of planar Li deposition induced by layered Ti_2C_3-T. (a) and (c) Adsorption energy of Ti_3C_2–O and Ti_3C_2–F sections to different Li layers. (b) and (d) Side view of the different charge densities of Li layer number deposition on the outer surface of Ti_3C_2-T ($X = O$, F). The loss of electrons is indicated in blue, and the gain of electrons is indicated in yellow.

thermodynamically LAGP is highly reactive with Li. The chemical reaction products of LATP/Li at a molar ratio of 0.07 are Li_3PO_4, Li_5AlO_4, Li_3P, and Ge. TEM was used to characterize the morphology evolution and interfacial stability of LAGP/MXene after 50 cycles. The cycled MXene shows integrated morphology with LAGP particles embedded in it (Fig. 7c). The crystalline structure was checked by HRTEM, and inter-

planes with distances of 0.36 nm and 0.99 nm are observed (Fig. 7d), corresponding to LAGP (113) and Ti_3C_2-T(002), respectively. The reactive nature/in situ formed protecting interphases between LAGP and Li metal was further confirmed by the TEM images of cycled LAGP particles, as shown in Fig. 7e. In situ formed nanocrystals are found, and the whole particle transformed into a porous morphology. The reaction between LAGP and Li metal induces a large mechanical stress and laterally causes a porous structure [38]. As a result, the LAGP accommodates the mechanical stress of Li dendrite growth and avoids its penetration into the PP separator through a reactive method. Even after 500 cycles, LAGP still exhibits an integrated particle morphology (Figure S12), implying the structural stability of LAGP during long-term cycling. The reaction products of LAGP/Li consist of Li_3PO_4 and Ge, as determined from the HRTEM image of cycled LAGP (Fig. 7f), which is consistent with the DFT calculation results. Considering the lithiation voltage of Ge starts at $\sim$ 0.5 V vs. Li/Li$^+$ [39], so $LiGe_x$ alloy may form during charge process. The mixed conductive Li_3PO_4 and Ge/$LiGe_x$ nanocrystals should facilitate fast lithium-ion and electron transportation through the interfaces of LAGP/MXene and Li metal.

X-ray photoelectron spectroscopy (XPS) was further performed to analyze the surface products of the protection layer between LAGP/MXene and Li metal. The C1s spectra of the pristine sample show two main peaks located at 285.6 eV and 290.1 eV (Fig. 7g), corresponding to C–O and C-F bonds [40], respectively. After cycling, these two peaks shift to lower binding energies; for example, new peaks at 284.3 eV ($C = C$) and 289.3 eV (C-F) are observed [40], indicating that the surface O and F functional groups were reduced by lithium atoms. For the F1s spectra (Fig. 7h), the same phenomenon is observed. In addition to the pristine C-F peak (687.1 eV), a new peak at 684.4 eV corresponding to Li-F is detected [41]. For the Ge3d spectrum (Fig. 7i), the main peak of LAGP (33.0 eV) is shifted to 29.3 eV, implying the reduction of LAGP and the formation of Ge nanoparticles [42], which is consistent with the TEM results. For the P2p spectra (Fig. 7j), the binding energy shifted from 133.9 eV to 133.2 eV, revealing the formation of Li_3PO_4 and Li_3P [42]. The XPS data further confirm that the surface O and F functional groups effectively reduce the energy barrier and provide nucleation sites for Li atoms, which laterally induces planar Li metal deposition on T_3C_2-T.
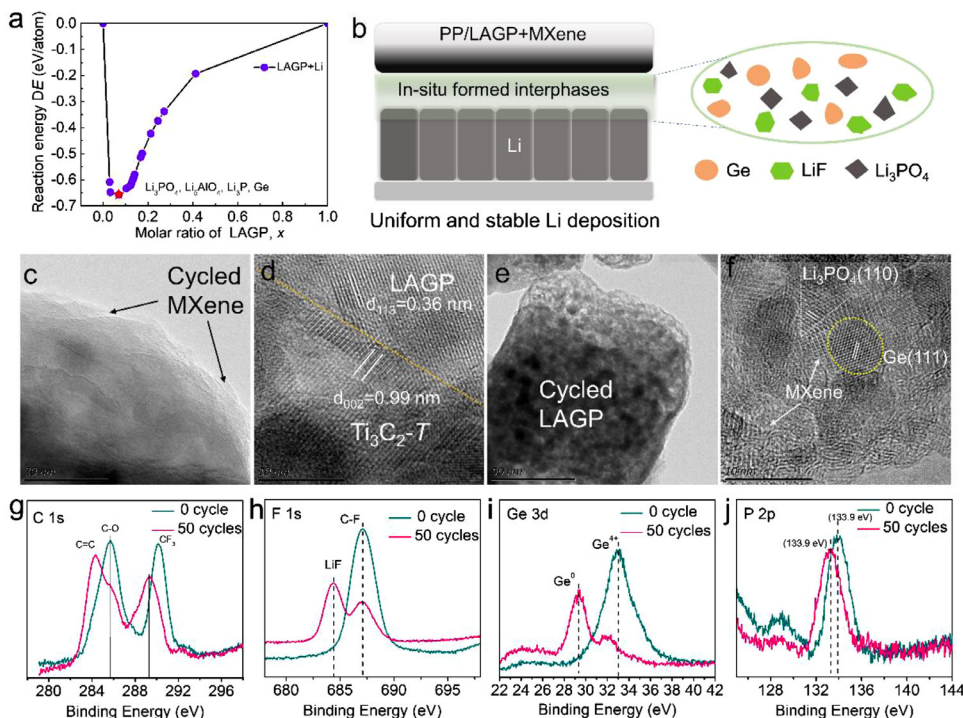
Fig. 7. Theoretical and experimental data reveal the nature of interphases formed in situ. (a) The reaction energy between LAGP and Li metal at different molar ratios. (b) Schematic of in situ formed interphases between LAGP/MXene and Li metal. (c) TEM image of cycled MXene. (d) HRTEM image at the interface between LAGP and Ti_3C_2-T. (e) TEM image of cycled LAGP particle. (f) HRTEM image of cycled LAGP particle. XPS analysis of LAGP/MXene before and after 50 cycles: (g) C1s, (h) F1s, (i) Ge3d, and (j) P2p.

The highly reactive nature of LAGP with Li metal helps to form a conductive and stable protection layer comprising Ge, Li_3PO_4, and Li_3P.

3. Conclusion

In summary, a universal strategy for separator modification that induces planar Li metal deposition with an engineered SEI layer is successfully proposed. T_3C_2-T with functional O and F groups provides effective initial nucleation sites, and the Li atom arrangement on T_3C_2-T surfaces inherits the MXene crystal structure, resulting in planar Li metal deposition at the bottom side. In addition, the reactive nature of LAGP helps to form an in situ protective layer comprising Ge, Li_3PO_4, and LiF. Furthermore, the mixed conductive nature of MXene/LAGP enables fast and uniform Li-ion/electron transfer at the interfaces. Taking advantage of the synergetic effects, the modified separator exhibits superior electrochemical performance in both half and full lithium metal cells. At a high area loading of 20 mg cm^{-2} LCO, the full cell exhibits stable cycling performance after 200 cycles. This work sheds light on the design of functional separators for high-performance Li metal batteries.

Experimental section

Materials synthesis: NASICON-type $Li_{1.3}Al_{0.3}Ge_{1.7}(PO_4)_3$ (LAGP) was synthesized by a solid-state reaction method. The starting materials were $LiOH·H_2O$ (99.95%, Sigma Aldrich), Al_2O_3 (99.99%, Sigma Aldrich), GeO_2 (99.8%, Sigma Aldrich), and $NH_4H_2PO_4$ (99.5%, Sigma Aldrich) powders. $LiOH·H_2O$ was heated at 250 °C for 3 h to remove crystalline H_2O prior to use. Stoichiometric amounts of chemicals with 10 wt.% excess LiOH were hand-ground for 0.5 h in an agate mortar. The mixed powders were then cold pressed into pellets with diameters of 13 mm at 400 MPa. The pellets were then preheated at 400 °C in air for 5 h, hand-ground into fine powders, cold pressed into pellets and sintered at 900 °C for 5 h. The synthesized LAGP pellet was ball milled (600/min for 3 h) into nanoparticles. For the preparation of MXene, 2 g of Ti_3AlC_2 powder (11 Technology Co., Ltd) was etched in 40% hydrofluoric acid (HF) and stirred for 10 h. Then, the etching solution was centrifuged several times until the pH reached 6. The as-received products were then ultrasonically treated in deionized water for 10 min. The solution containing MXene was then centrifuged 3 times. The MXene was carefully collected from the tube and stored in a vacuum oven.

The coating was created by slurry coating with a doctor blade. The slurry with 80 wt.% LAGP nanopowders, 10 wt.% MXene and 10 wt.% polyvinylidene fluoride (PVDF) binder was thoroughly mixed in 1-methyl-2-pyrrolidone (NMP) solvent. The well-dispersed slurry was then cast on commercial polypropylene (PP) separators dried in vacuum at 55 °C for 12 h. The coating thickness was controlled to be below 10 μm.

Characterization: The phase compositions of the synthesized LAGP powders, MXene and their composite were characterized by X-ray diffraction (XRD) (Cu K_α, $\lambda \sim 0.15406$ nm). Morphologies of the LAGP/MXene were examined using a field-emission scanning electron microscope (FESEM, JSM-7600F). The microstructures and compositions of MXene and LAGP before and after cycling were analyzed by a transmission electron microscope (TEM) equipped with an energy dispersive spectroscopy (EDS) (FEI Titan 300 kV). Atomic force microscopy (AFM, Bruker Dimension Edge) was used to detect the local surface morphology and electrical field distribution of the different separators.

Electrochemical evaluation: A carbonate electrolyte containing 1 M $LiPF_6$ in mixed EC/EMC/DMC (1:1:1 wt.%) solvents with 2 wt.% FEC additive was used and the amount is 80 μL for each cell. For ionic conductivity test, ions-blocking stainless steel (SS) was used as current collector and SS/separator/SS cells fabricated. Li/Li symmetric cells with PP and double-coated PP/LAGP+MXene separators were prepared with current densities between 1 and 5 mA cm^{-2}. Li/Cu cells with PP and single-coated PP/LAGP+MXene separators were also provided. Li/LCO cells with an active material loading of 20 mg cm^{-2} were fabricated and tested between 2.8–4.2 V. The long-life performance was tested at a rate

of 0.5C ($C = 140$ mA g^{-1}). Rate capability tests at various current densities from 0.5 to 4C were performed. Electrochemical impedance spectroscopy (EIS) tests were performed using an electrochemical workstation (Biologic SP-300) between 7 MHz and 0.1 Hz with an AC amplitude of 10 mV. CV curves of LCO/Li cells with PP and PP/LAGP+MXene separators were recorded between 2.8–4.2 V at a scan rate of 0.2 mV s^{-1}.

Computational method: All calculations were performed with the Vienna *ab initio* Simulation Package (VASP) based on density functional theory (DFT) [43] within the generalized gradient approximation of Perdew-Burke-Ernzerhof (PBE) [44]. The interaction between ion cores and valence electrons was treated using the projector augmented wave (PAW) method [45]. An energy cutoff of 500 eV was applied for the plane-wave expansion of the electronic eigenfunctions. The structures were relaxed until all the atomic forces on each ion were less than 0.01 eV/Å, and the energy convergence with the energy difference was below 10^{-5} eV. The vacuum space in the z direction was approximately 18 Å to avoid the interaction between adjacent sheets due to the periodic image. The Brillouin zones were sampled with a $2 \times 2 \times 1$ k-point mesh by the Monkhorst–Pack grid for Ti_3C_2-T (T = -O and -F) optimization. Throughout the simulations, van der Waals (vdW) interactions at the DFT-D2 level were taken into account [46].

The adsorption energies of different Li layer numbers on Ti_3C_2-T sections were calculated on a 3×3 supercell by

$$E_{ad} = \left[E(Ti_3C_2 - T + nLi) - E(Ti_3C_2 - T) - n\mu(Li) \right]/n,$$

where $E(Ti_3C_2$-$T+nLi)$ and $E(Ti_3C_2$-$T)$ are the total energies of Ti_3C_2-T with and without Li layer numbers, respectively; and $\mu(Li)$ is the chemical potential of Li obtained from the body-centered cubic (BCC) bulk structures of Li.

To obtain a mechanistic understanding of the charge transfer process of Li atom layer deposition on Ti_3C_2-T sections, a charge difference plot was used, and the charge difference was calculated by

$$\Delta\rho(r) = \rho_{Ti_3C_2-T+Li}(r) - \rho_{Ti_3C_2-T}(r) - \rho_{Li}(r),$$

where $\rho_{Ti_3C_2-X+Li}(r)$ represents the charge density of Li atom layer deposition on Ti_3C_2-T sections, $\rho_{Ti_3C_2-X}(r)$ is the charge density of Ti_3C_2-T, and $\rho_{Li}(r)$ is the charge density of isolated Li atoms in the same position as in the total systems.

To evaluate whether the LAGP/Li interfaces were thermodynamically favorable, we calculated the decomposition reaction energy of the LAGP reaction with metallic lithium by the reduction and decomposition of LAGP [47]. Here, we considered the interface to be a pseudo-binary system composed of LAGP and Li, x·LAGP + $(1 - x)$·Li. The pseudobinary phase diagrams were extracted from the multidimensional phase diagrams by taking the compositions of the LAGP and Li to each end point. The reaction energies of mutual decomposition at interface ΔE were determined by considering the mixing ratio x that yielded the largest reaction driving force [48,49], namely,

$$\Delta E(c_{Li}, c_{LAGP}) = \min_{x\in[0,1]} \left\{ \sum_i E(c_i) - [(1-x)E(c_{Li}) + xE(c_{LAGP})] \right\},$$

where $E(C_{Li})$ and $E(C_{LAGP})$ are the corresponding convex-hull minimum energies and $E(C_i)$ is the convex-hull function returning the lowest energy equilibrium of the phase at the given composition. The mutual reaction energies and equations are a function of the mixing ratio at this interface x, and x varies from 0 to 1.

Credit author contribution statement

X.H. and J.Z.C. conceived the idea and experiments; M.F.C and G.W.W. conducted the synthesis of MXene; W.J.Z. conducted the fabrication of LAGP, X.H., W.J.Z. and M.F.C carried out electrochemical performance testing, SEM, XPS, and AFM characterization; B.L. and S.Q.S. designed and conducted theoretical calculations; X.Y.Z. L.S.L. and S.Y.C. participated in the data analysis and discussion; C.P.W. supervised the project. All authors discussed the results and commented on the manuscript.

Supporting information

Supporting Information is available from the online version or from the author.

Declaration of Competing Interest

The authors declare that they have no known competing financial interests or personal relationships that could have appeared to influence the work reported in this paper.

Acknowledgements

Supplementary materials

Supplementary material associated with this article can be found, in the online version, at doi:10.1016/j.ensm.2021.04.029.

References

[1] X.B. Cheng, R. Zhang, C.Z. Zhao, Q. Zhang, Toward safe lithium metal anode in rechargeable batteries: a review, Chem. Rev. 117 (2017) 10403–10473.

[2] D. Lin, Y. Liu, Y. Cui, Reviving the lithium metal anode for high-energy batteries, Nat. Nanotechnol. 12 (2017) 194–206.

[3] B. Liu, J.G. Zhang, W. Xu, Advancing lithium metal batteries, Joule 2 (2018) 833–845.

[4] R. Zhang, N.W. Li, X.B. Cheng, Y.X. Yin, Q. Zhang, Y.G. Guo, Advanced micro/nanostructures for lithium metal anodes, Adv. Sci. 4 (2017) 1600445.

[5] Y. Guo, H. Li, T. Zhai, Reviving lithium-metal anodes for next-generation high-energy batteries, Adv. Mater. 29 (2017) 1700007.

[6] X. Zhang, Y. Yang, Z. Zhou, Towards practical lithium-metal anodes, Chem. Soc. Rev. 49 (2020) 3040–3071.

[7] Y. Ding, X. Guo, Y. Qian, H. Gao, D.H. Weber, L. Zhang, G. Yu, In situ formation of liquid metals via galvanic replacement reaction to build dendrite-free alkali-metal-ion batteries, Angew. Chem. 132 (2020) 12268–12275.

[8] J.B. Goodenough, Y. Kim, Challenges for rechargeable Li batteries. *Chemistry of materials*, Chem. Mater. 22 (2010) 587–603.

[9] Y. Zhang, T.T. Zuo, J. Popovic, K. Lim, Y.X. Yin, J. Maier, Y.G. Guo, Towards better Li metal anodes: challenges and strategies, Mater. Today 33 (2020) 56–74.

[10] W.W. Wang, Y. Gu, H. Yan, S. Li, J.W. He, H.Y. Xu, B.W. Mao, Evaluating solid–electrolyte interphases for lithium and lithium-free anodes from nanoindentation features, Chem 6 (2020) 2728–2745.

[11] C.Z. Zhao, P.Y. Chen, R. Zhang, X. Chen, B.Q. Li, X.Q. Zhang, X.B. Cheng, Q. Zhang, An ion redistributor for dendrite-free lithium metal anodes, Sci. Adv. 4 (2018) eaat3446.

[12] X. Fu, C. Shang, M. Yang, E.M. Akinoglu, X. Wang, G. Zhou, An ion-conductive separator for high safety Li metal batteries, J. Power Sources 475 (2020) 228687.

[13] X. Han, Y. Gong, K.K. Fu, X. He, G.T. Hitz, J. Dai, L. Hu, Negating interfacial impedance in garnet-based solid-state Li metal batteries, Nat. Mater. 16 (2017) 572–579.

[14] D. Wang, W. Zhang, W. Zheng, X. Cui, T. Rojo, Q. Zhang, Towards high-safe lithium metal anodes: suppressing lithium dendrites via tuning surface energy, Adv. Sci. 4 (2017) 1600168.

[15] R. Wen, Y.G. Guo, L.J. Wan, Synergism of Al-containing solid electrolyte interphase layer and Al-based colloidal particles for stable lithium anode, Nano Energy 36 (2017) 411–417.

[16] J. Guo, Z. Wen, M. Wu, J. Jin, Y. Liu, Vinylene carbonate-LiNO$_3$: a hybrid additive in carbonic ester electrolytes for SEI modification on Li metal anode, Electrochem. Commun. 51 (2015) 59–63.

[17] R. Miao, J. Yang, X. Feng, H. Jia, J. Wang, Y. Nuli, Novel dual-salts electrolyte solution for dendrite-free lithium-metal based rechargeable batteries with high cycle reversibility, J. Power Sources 271 (2014) 291–297.

[18] M.S. Kim, J.H. Ryu, Y.R.Lim Deepika, I.W. Nah, K.R. Lee, L.A. Archer, W.I. Cho, Langmuir–Blodgett artificial solid-electrolyte interphases for practical lithium metal batteries, Nat. Energy 3 (2018) 889–898.

[19] X. Liang, Q. Pang, I.R. Kochetkov, M.S. Sempere, H. Huang, X. Sun, L.F. Nazar, A facile surface chemistry route to a stabilized lithium metal anode, Nat. Energy 2 (2017) 1–7.

[20] Y. Gao, Z. Yan, J.L. Gray, X. He, D. Wang, T. Chen, Q. Huang, Y.C. Li, H. Wang, S.H. Kim, T.E. Mallouk, D. Wang, Polymer–inorganic solid–electrolyte interphase for stable lithium metal batteries under lean electrolyte conditions, Nat. Mater. 18 (2019) 384–389.

[21] Y. Gu, W.W. Wang, Y.J. Li, Q.H. Wu, S. Tang, J.W. Yan, M.S. Zheng, D.Y. Wu, C.H. Fan, W.Q. Hu, Z.B. Chen, Y. Fang, Q.H. Zhang, Q.F. Dong, B.W. Mao, Designable ultra-smooth ultra-thin solid-electrolyte interphases of three alkali metal anodes, Nat. Commun. 9 (2018) 1–9.

[22] A. Wang, S. Tang, D. Kong, S. Liu, K. Chiou, L. Zhi, J. Huang, Y.Y. Xia, J. Luo, Bending-tolerant anodes for lithium-metal batteries, Adv. Mater. 30 (2018) 1703891.

[23] C.P. Yang, Y.X. Yin, S.F. Zhang, N.W. Li, Y.G. Guo, Accommodating lithium into 3D current collectors with a submicron skeleton towards long-life lithium metal anodes, Nat. Commun. 6 (2015) 1–9.

[24] T. Zhou, J. Shen, Z. Wang, J. Liu, R. Hu, Regulating lithium nucleation and deposition via MOF-derived Co@ C-Modified carbon cloth for stable Li metal anode, Adv. Funct. Mater. 30 (2020) 1909159.

[25] S.H. Wang, Y.X. Yin, T.T. Zuo, W. Dong, J.Y. Li, J.L. Shi, C.H. Zhang, N.W. Li, C.J. Li, Y.G. Guo, Stable Li metal anodes via regulating lithium plating/stripping in vertically aligned microchannels, Adv. Mater. 29 (2017) 1703729.

[26] Y. Guo, P. Niu, Y. Liu, Y. Ouyang, D. Li, T. Zhai, H. Li, Y. Cui, An autotransferable g-C$_3$N$_4$ Li$^+$–modulating layer toward stable lithium anodes, Adv. Mater. 31 (2019) 1900342.

[27] Q. Yang, Z. Huang, X. Li, Z. Liu, H. Li, G. Liang, D. Wang, Q. Huang, S. Zhang, S. Chen, A wholly degradable, rechargeable Zn–Ti$_3$C$_2$ MXene capacitor with superior anti-self-discharge function, ACS Nano 13 (2019) 8275–8283.

[28] Y. Gogotsi, B. Anasori, The rise of MXenes, ACS Nano 13 (2019) 8491–8494.

[29] Z. Cao, Q. Zhu, S. Wang, D. Zhang, H. Chen, Z. Du, S. Yang, Perpendicular MXene arrays with periodic interspaces toward dendrite-free lithium metal anodes with high-rate capabilities, Adv. Funct. Mater. 30 (2020) 1908075.

[30] H. Shi, M. Yue, C.J. Zhang, Y. Dong, P. Lu, S. Zheng, Z.S. Wu, 3D Flexible, Conductive, and recyclable Ti$_3$C$_2$T$_x$ MXene-melamine foam for high-areal-capacity and long-lifetime alkali-metal anode, ACS Nano 14 (2020) 8678–8688.

[31] C. Wei, Y. Tao, Y. An, Y. Tian, Y. Zhang, J. Feng, Y. Qian, Recent advances of emerging 2D MXene for stable and dendrite-free metal anodes, Adv. Funct. Mater. 30 (2020) 2004613.

[32] X. Jiang, S. Liu, W. Liang, S. Luo, Z. He, Y. Ge, H. Zhang, Broadband nonlinear photonics in few-layer MXene Ti$_3$C$_2$T$_x$ (T= F, O, or OH), Laser Photonics Rev. 12 (2018) 1700229.

[33] P. Maldonado-Manso, E.R. Losilla, M. Martínez-Lara, M.A. Aranda, S. B ue, F.E. Mouahid, M. Zahir, High lithium ionic conductivity in the Li$_{1+x}$Al$_x$G$_y$Ti$_{2-x-y}$(PO$_4$)$_3$ NASICON series, Chem. Mater. 15 (2003) 1879–1885.

[34] M.R. Busche, T. Drossel, T. Leichtweiss, D.A. Weber, M. Falk, M. Schneider, J. Janek, Dynamic formation of a solid-liquid electrolyte interphase and its consequences for hybrid-battery concepts, Nat. Chem. 8 (2016) 426–434.

[35] H. Wang, Y.H. Li, Y.B. Li, Y. Liu, D. Lin, C. Zhu, Y. Cui, Wrinkled graphene cages as hosts for high-capacity Li metal anodes shown by cryogenic electron microscopy, Nano Lett 19 (2019) 1326–1335.

[36] Y. Gao, Z.F. Yan, J.L. Gray, X. He, D.W. Wang, T. Chen, D.H. Wang, Polymer–inorganic solid–electrolyte interphase for stable lithium metal batteries under lean electrolyte conditions, Nat. Mater. 18 (2019) 384–389.

[37] J. Betz, G. Bieker, P. Meister, T. Placke, M. Winter, R. Schmuch, Theoretical versus practical energy: a plea for more transparency in the energy calculation of different rechargeable battery systems, Adv. Energy Mater. 9 (2019) 1803170.

[38] J.P. Zhu, J. Zhao, Y.X. Xiang, M. Lin, H.C. Wang, B.Z. Zheng, H.J. He, Q.H. Wu, J.Y. Huang, Y. Yang, Chemo-mechanical failure mechanism study in NASICON-type Li$_{1.3}$Al$_{0.3}$Ti$_{1.7}$(PO$_4$)$_3$ solid-state lithium batteries, Chem. Mater 32 (2020) 4998.

[39] X. Liu, X.Y. Wu, B. Chang, K.X. Wang, Recent progress on germanium-based anodes for lithium ion batteries: efficient lithiation strategies and mechanisms, Energy Storage Mater 30 (2020) 146–149.

[40] T. Wang, Y. Li, K.Yan J.Zhang, P. Jaumaux, J. Yang, G. Wang, Immunizing lithium metal anodes against dendrite growth using protein molecules to achieve high energy batteries, Nat. Commun. 11 (2020) 1–9.

[41] Y. Zhou, X. Zhang, Y. Ding, J. Bae, X. Guo, Y. Zhao, G. Yu, Redistributing Li-ion llux by parallelly aligned holey nanosheets for dendrite-free Li metal anodes, Adv. Mater. 32 (2020) 2003920.

[42] L. He, Q. Sun, C. Chen, J. Oh, J. Sun, M. Li, L. Lu, Failure mechanism and interface engineering for NASICON-structured all-solid-state lithium metal batteries, ACS Appl. Mater. Interfaces 11 (2019) 20895–20904.

[43] G. Kresse, J.F. l., Efficient iterative schemes for ab initio total-energy calculations using a plane-wave basis set, Phys. Rev. B 54 (1996) 11169–11186.

[44] J.P. Perdew, K. Burke, M. Ernzerhof, Generalized gradient approximation made simple, Phys. Rev. Lett. 77 (1996) 3865–3868.

[45] P.E. Blöchl, Projector augmented-wave method, Phys. Rev. B 50 (1994) 17953.

[46] S. Grimme, Accurate description of van der waals complexes by density functional theory including empirical corrections, J. Comput. Chem. 25 (2004) 1463–1473.

[47] B. Liu, J. Yang, H. Yang, C. Ye, Y. Mao, J. Wang, S. Shi, J. Yang, W. Zhang, Rationalizing the interphase stability of Li| doped-Li$_7$La$_3$Zr$_2$O$_{12}$ via automated reaction screening and machine learning, J. Mater. Chem. A 7 (2019) 19961–19969.

[48] B. Liu, J. Liu, J. Yang, D. Wang, C. Ye, D. Wang, M. Avdeev, S. Shi, J. Yang, W. Zhang, Ab initio thermodynamic optimization of Ni-rich Ni–Co–Mn oxide cathode coatings, J. Power Sources 450 (2020) 227693.

[49] S. Shi, J. Gao, Y. Liu, Y. Zhao, Q. Wu, W. Ju, R. Xiao, Multi-scale computation methods: their applications in lithium-ion battery research and development, Chinese Physics B 25 (2016) 018212.